Nanoscale

Accepted Manuscript

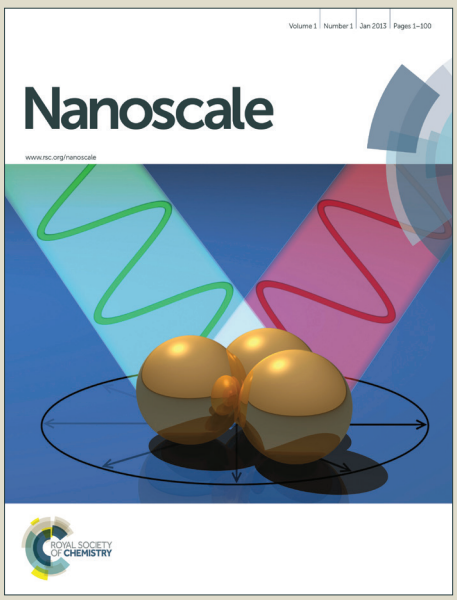

ROYAL SOCIETY OF CHEMISTRY

www.rsc.org/nanoscale

Nanoscale

RSCPublishing

ARTICLE

Reduced Graphene Oxides: The Thinnest and Most Lightweight Material with High-efficient Microwave Attenuation Performances around Carbon World

B. Wen,[a,1] X. X. Wang,[a,1] W. Q. Cao,[b] H. L. Shi,[b] M. M. Lu,[a] G. Wang,[a] H. B. Jin,[a,*] W. Z. Wang,[b,*] J. Yuan[b] and M. S. Cao[a,*]

Cite this: DOI: 10.1039/x0xx00000x

Received 00th January 2012,
Accepted 00th January 2012

DOI: 10.1039/x0xx00000x

www.rsc.org/

In this work, reduced graphene oxide (r-GO) and graphite nanosheet (GN) were achieved via chemical approach. Furthermore, r-GO composites and GN composites with paraffin wax host were prepared, respectively. R-GO composites show high dielectric property and electromagnetic interference shielding efficiency (EMI SE). Compared to the GN composites, loss tangent and EMI SE of the r-GO composites with the same mass ratio enhance ~5–10 times and ~3–10 times, respectively. The enhanced attenuation capacity arises from higher specific surface area, clustered defects and residual bonds of the r-GOs, which increased the polarization loss, scattering and conductivity of the composite. Meanwhile, higher conductivity of r-GO composites leads to the higher EMI SE compared to the GN composites. The results suggest that the r-GOs are highly promising filler for microwave attenuation around carbon family. R-GO composite is a high-performance EMI shielding material anticipating for application in many fields.

Introduction

Development of materials with efficient microwave attention performances, which can protect our life against the electromagnetic (EM) wave, is highly demanded, particularly in our workplaces, launching from the good function of electronic equipment, such as the sensitive electronic circuits of the computers. Nanoscale carbon materials, such as carbon nanocoil (CNC), carbon nanotube (CNT), graphite nanosheet (GN) and carbon nanofiber (CNF), are superior for achieving highly efficient microwave attenuation composites with lightweight, wide absorption frequency range, and strong absorption capacity because of their high electron mobility, which lead to efficient electron transport in the micro-current network under the electric fields.[1-9]

In recent years, significant effort has been devoted to the graphene and chemically converted reduced graphene oxides (r-GOs), due to their novel properties.[10-12] Recent reports suggested that the graphene-based materials showed great potentials in electrical devices,[13-16] lithium-ion batteries,[17-22]electrocatalyst,[23-25]photoluminescence,[26,27] and thermal transport applications.[28,29] More recently, due to their fewer layers and excellent electrical properties, the microwave attenuation performances of the r-GO attract much attention in global in order to achieve high-performance electromagnetic interference (EMI) shielding material with lightweight and high efficiency.[30-34] However, the effect of the structure and microstructure of the r-GO on the microwave is unclear. Furthermore, the microwave attenuation performances of the r-GO-based composites are lack of sufficient theoretical support for advanced design and application in commercial fields.

Herein, single layer r-GOs are loaded into paraffin wax matrix to form composites. The dielectric properties and microwave attenuation performances of the composites are studied. The results indicate that r-GO-based composites have high-performance EMI shielding efficiency (SE). The dielectric properties and attenuation mechanism are discussed in detail.

Results and discussion

Characterization

Graphite oxides were obtained by harsh oxidation of the natural graphite powders according to the modified Hummers' method.[35] And the r-GOs were produced by chemically reduction of the GOs with hydrazine hydrate. GNs were obtained by exfoliation of the graphite (Scheme 1).[2]

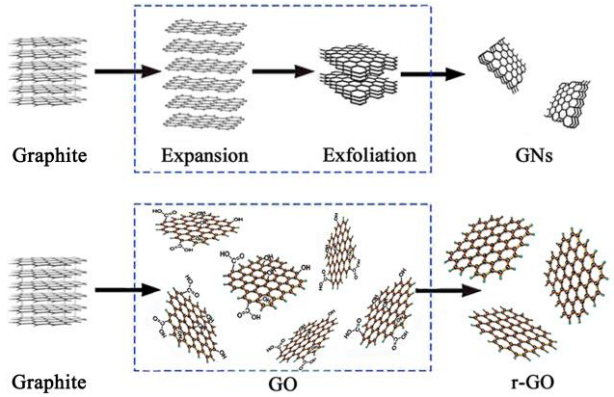

Scheme 1. Synthetic illustration of the GNs and r-GOs

Atomic force microscope (AFM) is used to assess the thickness of the GO and GN. the AFM image shown in Figure 1A suggests that the GO is on the order of 1~2 micron in size and less than 1.2 nm in height, indicating that the single layer r-GO was achieved.[36] GN is larger than GO in size and ~5 nm in height, showing that the prepared GN has the multi-layer structure as shown in Figure 1B.

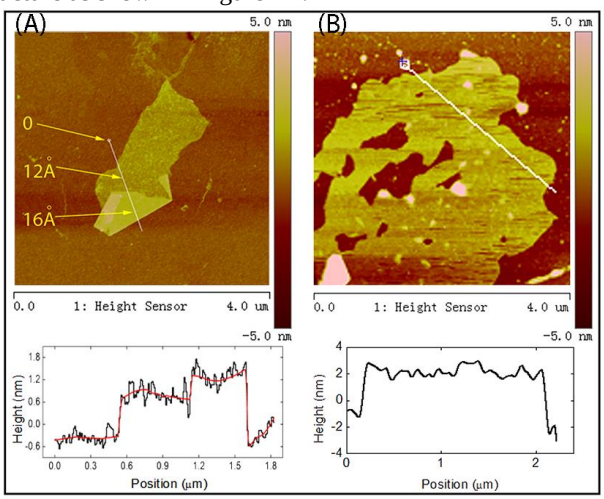

Figure 1. AFM images of the GO and GN.

The GN and r-GO were also characterized by the transmission electron microscope (TEM). As shown in Figure 2A, the different contrast in the edge indicates the multilayer structure of the GN, which is further indicated by the result of the high-resolution TEM (HRTEM) image as shown in Figure 2B. The image of the Figure 2C suggests that the r-GO layer is flexible and quite thin. Some part of the r-GO is folded via chemical convention process, which can be clearly seen in the amplified TEM image in Figure 2D. The selected area electron diffraction (SAED) patterns of the GN and r-GO along the [001] zone axis are showed in Figure 2E and F, respectively. The diffraction pattern of the GN depicted in Figure 2E shows a graphitic crystalline structure. The spots figured out by the red circles in Figure 2E illustrate the laminar structure of the GN. Figure 2F displays a weak graphitic crystalline structure pattern compared to the GN, due to the thinner thickness of the r-GO. As shown in Figure 2G, the GNs show typical graphitic peak centered at ~2θ = 26.5°, corresponding to the (002) interlayer reflection of graphitic layers.[36] Furthermore, the peak width of the GNs is broadened compared to the peak width of the natural graphite, indicating a dramatic decrease in the thickness of GNs.[2] After harsh oxidization, a strong characteristic peak appears at ~2θ = 11.5°, and no obvious graphite peaks appear in the obtained graphite oxides, indicating an increase in the interlayer distance caused by the formation of hydroxyl, epoxy and carboxyl groups on the graphene sheets. After chemically reduction, a broad peak of r-GOs appears at ~2θ = 23.9°, caused by the disorder of the graphene layers, which is in good agreement with the reported literature.[37] To characterize the structure of the r-GO further, the profile X-ray diffraction (XRD) of the GN and r-GO is obtained by a profile tool in the Digital Micrograph based on the SAED patterns as shown in Figure 2H.[38] Attributed to the advantages of the TEM, the profile XRD can show the microstructure more clearly, rather than the average information got in the routine XRD experiments. Due to the extremely thin thickness of the r-GO, the profile intensity of the r-GO is weak. But the peaks of the GN and r-GO at ~2θ = 42.76° are in the same position as shown in Figure 2H, indicating the graphitic crystalline structure of the r-GO.

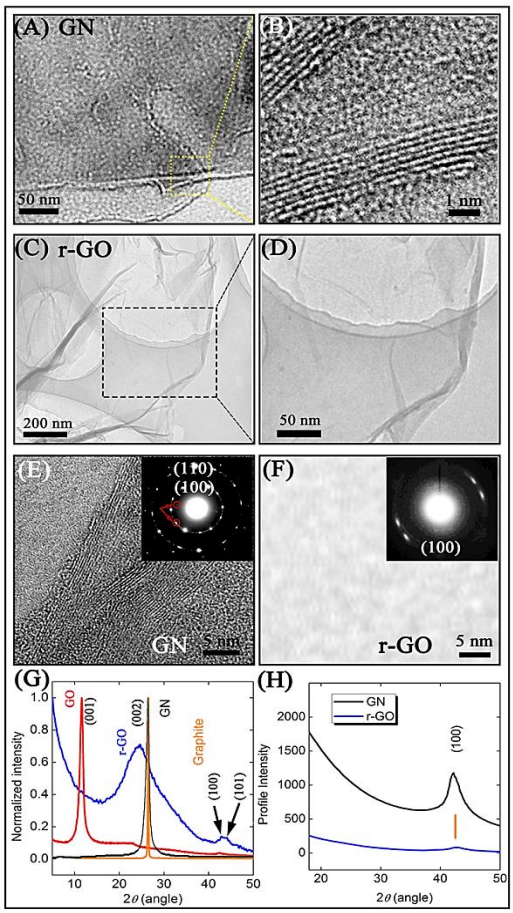

Figure 2. (A, B) TEM and HRTEM images of the GN. (C, D) TEM images of the r-GO. (E, F) SAED patterns of the GN and r-GO. (G) Powder XRD patterns of the GO, r-GO, GN and graphite. (H) Profile XRD patterns of the GN and r-GO.

The volumes of the GNs and r-GOs with the same weight are observed directly. As shown in Supplementary Figure S1, the volume of the r-GOs is ~8 times larger than that of the GNs. Furthermore, the specific surface areas (SSA) of GN and r-GO were determined by N_2 adsorption/desorption analysis (Figure S2 and Table S1). The SSA of the r-GOs is much higher than that of the GNs, which would significant improved the EM wave

attenuation of the composites filled with high-SSA materials.

Microwave attenuation performances

Coefficients of absorption (*A*), reflection (*R*), and transmission (*T*) In order to investigate the microwave attenuation performances of the r-GO composites, the scattering parameters (S_{11} and S_{21}) were measured by a vector network analyzer system to calculate the *A*, *R* and *T* coefficients of the r-GO and GN composites. The plotted curves, which show the r-GO composites compared to the GN composites, aim to show the excellent EM wave attenuation performances of the r-GO composites with changing frequency and mass ratio.

Figure 3 shows the calculated *A* values of the r-GO and GN composites with a thickness of 2 mm in the frequency range of 2–18 GHz. As revealed in Figure 3A and B, the *A* values of the r-GO and GN composites increase with increasing mass ratio, and reach the maximal values ~0.75 and ~0.53, respectively. According to the plots as exhibited in Figure 3A, the *A* values of the r-GO composites are in the range of 0.38~0.75. Almost half of the total area of the *A* projection is above 0.5, which is much higher than *A* values of the GN composites. Furthermore, the r-GO composites demonstrate much improved absorption performance compared to GN as shown in Figure 3C–F. The *A* values of the r-GO composites enhance ~1–15 times than that of GN composites. Moreover, the *A* values of the r-GO composites increase with increasing frequency (Figure 3C–F), which are attributed to the increased effective thickness of the composites with decreasing wavelength.

The *R* values of the r-GO composites at each mass ratio are closed to that of the GN composites. Due to the similar two-dimensional (2D) structure of GN and r-GO as shown in Figure 1 and 2 above, the both graphene-based composites may construct similar surface impedance with the air, which tends to show the near *R* values (Figure 4A and B). The deviation of the *R* values between r-GO and GN composites is less than 30 percent (Figure 4C–F). The *R* values of the r-GO composites increase with increasing mass ratio, and decrease with increasing frequency. Furthermore, the *R* values of the r-GO composites change from 0.22 to 0.47 and 0.38 to 0.69 with 5 and 20 wt. % r-GO, respectively. These plots show that the trend of the *R* depends on the mass ratio and the frequency.

The increasing mass ratio of the r-GO and GN causes a substantially decrease of the *T* values of the composites as shown in Figure 5A and B. The *T* values of the r-GO composites are mostly lower than 0.1, which are also much lower than that of the GN composites as shown in Figure 5A. Furthermore, compared to the GN composites, the *T* values of the r-GO composites decrease with increasing mass ratio (Figure 5C–F). Specifically, the *T* values of the r-GO composite with 20 wt. % r-GOs are ~180 times lower than that of GN composite (Figure 5F). In other words, due to higher *A* and *R* coefficients, more EM wave is consumed by the r-GO composites, which leads to more significant decrease of the *T* values.

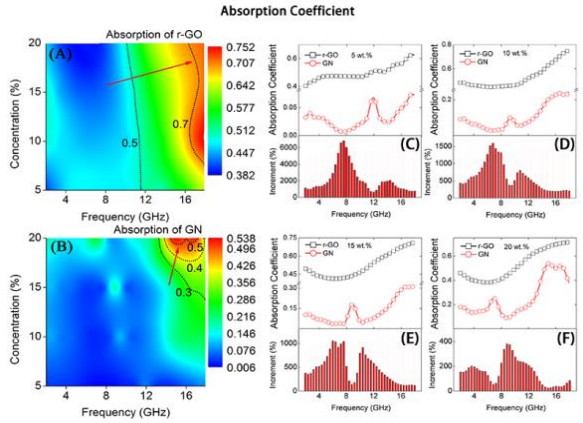

Figure 3. (A, B) absorption coefficient of the r-GO and GNs. (C, D, E, F) absorption comparison and increment of the r-GO and GN composites at each mass ratio.

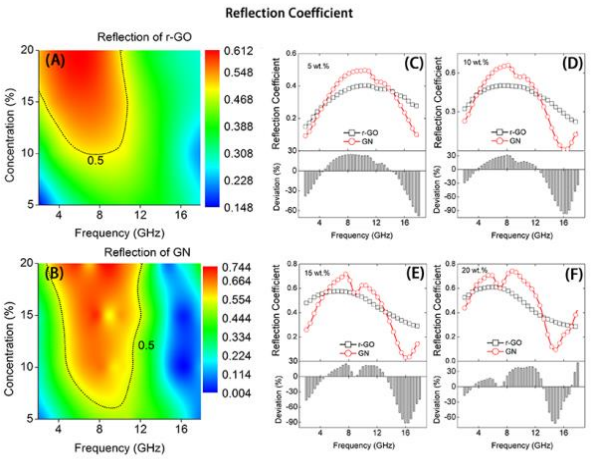

Figure 4. (A, B) reflection coefficient of the r-GO and GNs. (C, D, E, F) reflection comparison and deviation of the r-GO and GN composites at each mass ratio.

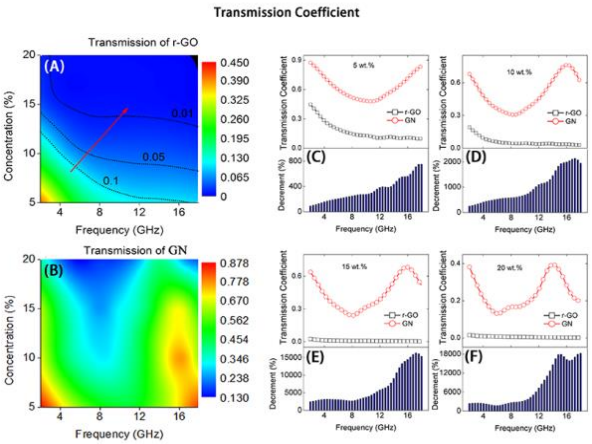

Figure 5. (A, B) transmission coefficient of the r-GO and GNs. (C, D, E, F) transmission comparison and decrement of the r-GO and GN composites at each mass ratio.

Permittivity and the Loss The coefficients of the *A*, *R* and *T* are determined by the dielectric properties, which are strongly depended on the SSA, electron mobility and microstructure of the fillers. According to the reported results in the literature,[39]

the defects in carbon nanotubes may construct localized states near to the Fermi level to increase the radiation attenuation. The microstructure investigations show that the r-GO contains clustered defects and residual bonds arising from oxidation process (seeing the XPS spectra showing in Figure S3).[40] There are more oxygenic functional groups on the r-GOs (Table S2), which might increase the EM wave attenuation performance. Meanwhile, because of the thinnest thickness and high electron mobility, r-GO has higher SSA and higher hopping conductivity, which induces strong polarization and loss conductance towards the EM wave. The complex permittivity reflects the polarization and loss of the fillers to the EM wave. So the complex permittivity of the GN and r-GO composites was investigated on the vector network analyzer by the coaxial line method. As shown in Figure 6 and 7, the permittivity (real part ε' and imaginary part ε'') and loss tangent ($\tan\delta = \varepsilon''/\varepsilon'$) of GN and r-GO composites with the same mass ratio were obtained in the 2-18 GHz frequency range.

In Figure 6A, the ε' values of the r-GO composites are generally higher than that of the GN composites with corresponding mass ratio. Meanwhile, the ε' of the r-GO composites decreases more quickly than that of the GN composites with increasing frequency. It is found that the ε' values of the both composites obviously increase with increasing mass ratio. The ε' values of the r-GO composites are in the range of 4.48–8.48, 6.67–13.12, 10.16–23.62, and 11.64–28.3 when load with 5, 10, 15 and 20 wt. % r-GOs, respectively. Since ε' is an expression of the polarization of a material, which consists of the interface polarization and orientation polarization under the EM field. As revealed in Scheme 2A and B, the thickness of the r-GO is much thinner than the GN, which leads to more charge carriers and interfaces in the r-GO composites resulting in higher ε' and obvious decrease with the increase of frequency (Figure 6A). Furthermore, as schematically shown in Scheme 2B, due to the residual bonds and clustered defects introduced via chemical conversion process, the electrons are not evenly distributed, leading to the orientation polarization which further enhances the ε'.

As shown in Figure 6B, the ε'' of the r-GO composites at each mass ratio is apparently higher than that of the GN composites. No obvious resonance peaks appear at the ε'' curves of the r-GO composites in Figure 6B. Moreover, the ε'' of the r-GO composites also increases with increasing mass ratio. The values of the ε'' are in the range of 2.08–4.42, 3.87–8.71, 8.2–24.39, and 10.93–28.73 with the same mass ratio as mentioned above, respectively. As shown in Figure 7A, the tanδ of the r-GO composites is ~5–10 times higher than that of the GN composites, indicating that the r-GO composites have much higher EM wave loss than the GN composites. The tanδ values of the r-GO composites is ≥1 when the mass ratio is higher than 15 wt. %, which is caused by the higher conductivity and polarization of the r-GOs as revealed in Scheme 2B. The dielectric loss of the composites could be explicated by the Debye theory.[3] The ε'' is shown as,

$$\varepsilon'' = (\varepsilon_s - \varepsilon_\infty)\times\omega\tau/(1+\omega^2\tau^2) + \sigma/\omega\varepsilon_0 \quad (1)$$

where the σ is the *dc* conductivity of the composites. Due to the recovery of the electric conductivity after chemical reduction and thinner thickness,[41-43] the increased polarization caused by abundant surface functional groups enhances the dielectric loss. On the other hand, r-GOs construct more conductive paths in the composites for electrons transporting (Scheme 2C and D), which makes a significant contribution to dielectric loss. GNs have higher conductivity than the r-GOs. Nevertheless, due to the fewer conductive paths inside the composites, the effective conductivity of the GN composites is much lower than that of the r-GO composites with the same mass ratio. Thus, the r-GO composites exhibit higher ε'' and tanδ values than the GN composites. In order to study the change of the σ clearly, the σ values of the r-GO and GNs composites are determined using the standard four-point contact method. As shown in Figure 7B, the σ values of the r-GO composites are much higher than that of GN composites at each mass ratio. The measured σ values consistent with our conductivity path model, as shown in Scheme 2C and D. While larger volume of the r-GOs makes a main contribution to get higher hopping conductivity. In addition, the r-GOs are folded and thinner than previous carbon materials. Therefore, the r-GOs are easier to link-up to form micro-current network compared to the GNs with the same mass ratio.

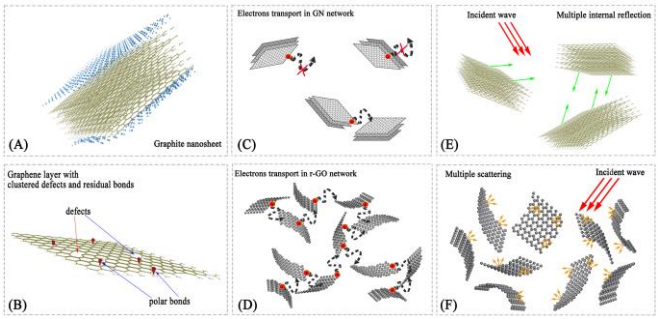

Scheme 2. (A, B) microstructure of the GN and r-GO (C, D) electrons transport network of the GN and r-GO (E, F) microwave propagation model in the GN and r-GO composites

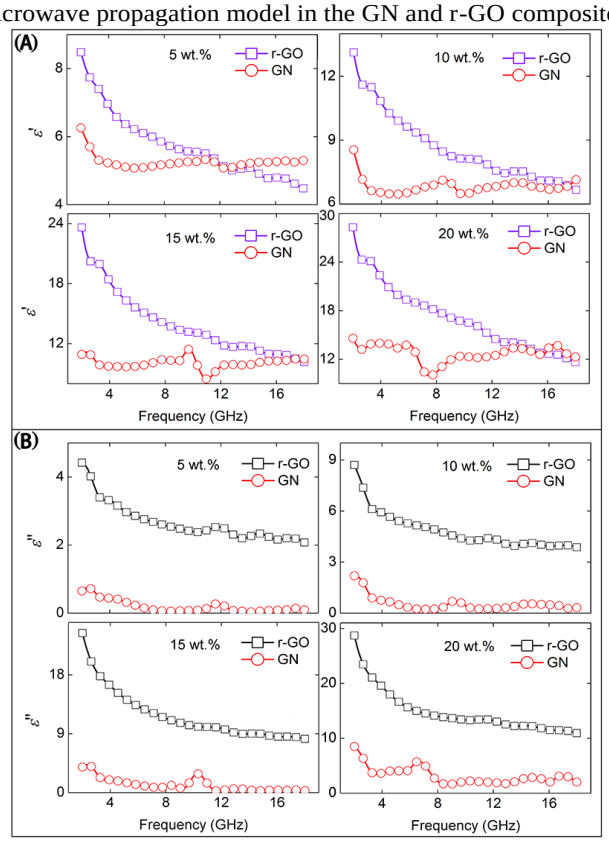

Figure 6. Comparison of the r-GO and GN composites vs. frequency (A) Real permittivity, and (B) imaginary permittivity.

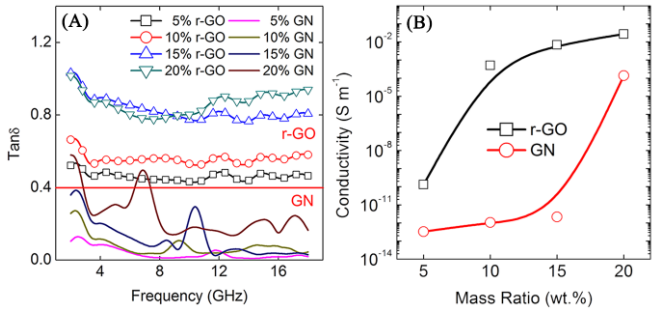

Figure 7. (A) tanδ of the r-GO and GN composites. (B) log10 DC conductivity (σ) vs. mass ratio of the r-GO/wax and GN/wax composites.

EMI SE The dielectric properties and attenuation performances of the composites determine the EMI shielding characteristics.[44-46] The SE in dB can be obtained by the equation as,[47-50]

$$\text{EMI SE} = 10\lg(P_I/P_T) = 10\lg(1/T) \quad (2)$$

where P_I and P_T are the power of the incident wave and the transmit wave that travel through the composites, respectively. The as-obtained SE towards EMI is shown in Figure 8. As observed from the three-dimensional (3D) SE plots in Figure 8A and B, the EMI SE of the r-GO and GN composites both depends on the frequency and mass ratio. The SE of the r-GO composites increases with increasing frequency; and is enhanced substantially by increasing mass ratio. Furthermore, compared to the GN composites, an enhancement factor at least~300% is obtained in the corresponding SE values of the r-GO composites (Figure 8C–F). The maximal SE values of r-GO composites with 5, 10, 15 and 20 wt. % r-GOs are 10.09, 15.24, 24.72 and 29.68 dB, respectively. The bandwidth of SE above 20 dB for the r-GO composites with 15 and 20 wt. % is in the range of 5.84–18 GHz and 3.36–18 GHz, respectively.

In general, the EMI shielding performances of the composites depend on the reflection from the material's surface, absorption of the EM energy, and propagation paths of the EM wave, which are determined by the nature, shape, size and microstructure of the fillers.[49] The R and A coefficients of the r-GO composites are high, indicating that the potential EMI shielding ability of the r-GO comprises is mainly from the reflection and absorption. In order to reveal the SE of reflection (SE_R) and absorption (SE_A) in detail, the SE in dB can also be obtained by the equation as,[51]

$$SE = SE_A + SE_R \quad (3)$$

The effective absorbance (A_{eff}) can be described as,[52,53]

$$A_{eff} = (1 - R - T)/(1 - R) \quad (4)$$

With respect to the power of the microwave in the composite, the reflection and effective absorption can be conveniently expressed as,[51,54]

$$SE_R = -10\lg(1 - R) \quad (5)$$

and

$$SE_A = -10\lg(1 - A_{eff}) = -10\lg[T/(1 - R)] \quad (6)$$

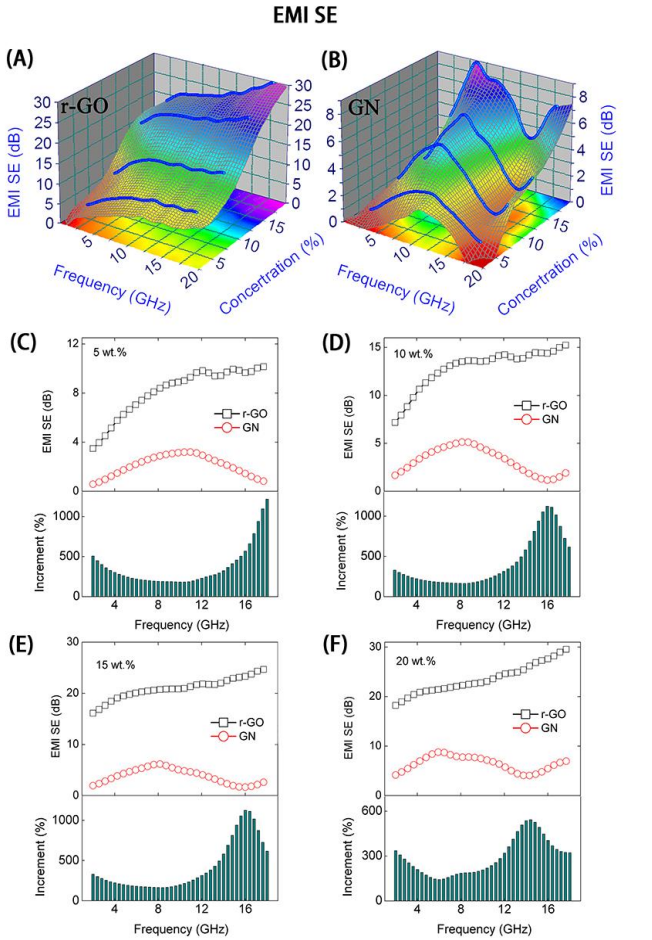

Figure 8. (A, B) EMI SE of the r-GO and GN composites, respectively. (C, D, E, F) comparison and increment SE of the r-GO and GN composites at each mass ratio.

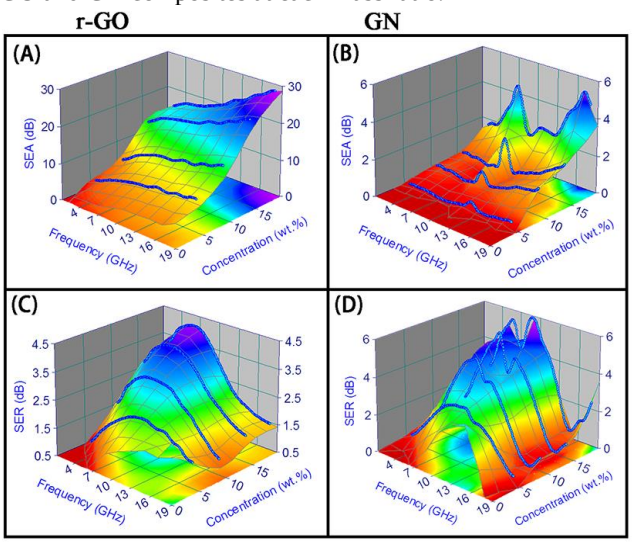

Figure 9. (A, B) SE_A of the r-GO and GN composites. (C, D) SE_R of the r-GO and GN composites.

The as-obtained SE_A and SE_R are plotted in Figure 9. From the sets of the Figure 9A, the SE_A values considerably increase with increasing mass ratio of the r-GOs over the entire frequency range. As shown in Figure 9A and B, the SE_A values of the r-

GO composites are much improved over the GN composites, which keep consistent with the *A* values above. The SE_A values of the composites with 5, 10, 15 and 20 wt. % r-GO are in the range of 2.78–8.69, 5.47–14.18, 13.28–23.26 and 15–28.22 dB, respectively. The SE_R values of the r-GO composites have a maximal value around 7 GHz, and the values of SE_R increase with increasing mass ratio (Figure 9C). In addition, as shown in Figure 9C and D, the SE_R values of the GN and r-GO composites are almost the same, where the deviations for the SE_R values are less than 1.5 dB. Due to the similar 2D structure of the fillers, the r-GO and GN composites may construct similar interface between air and the composites. Moreover, the SE_A values of the r-GO composites are higher than the SE_R values, indicating the primary absorption characteristic of the r-GO composites towards EM wave.

The dielectric properties and microwave attenuation capacity are associated with the microstructure of the fillers. In the present work, there are three main reasons for the enhanced microwave attenuation performances of the r-GO composites, which are presented in Scheme 2. Firstly, as mentioned above, the extremely thin and high polarity of the r-GO may offer more opportunities to induce polarization by EM wave, which improves both the ε' and ε''. Secondly, the decreased thickness of the r-GOs increases the conductive paths inside the composites, which leads to high-efficient microwave attenuation through the conversion of microwave into heat as illustrated in Scheme 2D.[55,56] The better dielectric property of the r-GO composites shown in Figure 3A and 3B provides a direct evidence that polarization has an important influence on the dielectric properties, and the conductivity of the composites achieved in the r-GOs is generally considered as a significant factor in the dielectric properties and corresponding microwave attenuation performances. And thirdly, the r-GOs are extremely thin, flexible and corrugated, which increases the propagation paths for the EM wave inside the composites as compared with GNs. As described in Scheme 2E and F, The EM wave scattered by corrugated graphene layers, has significantly enhanced attenuation performances than that of the GN composites with multiple internal reflection mode.

In addition, with increasing mass ratio of the r-GOs, the EMI SE of the composites increases. When the microwave propagates in the composites, the directional motion of the charge carriers in the r-GO network formed oscillatory current,[51,53] which would consume much EM wave energy. Thus, the increased scattering coupled with higher conductivity is responsible for the enhancement of the SE. Furthermore, sufficient states induced by defects and residual bonds in/on the r-GOs increase the absorption of the microwave. With high mass ratio of the r-GOs, conductivity plays the main role towards EM wave attenuation. Conductivity of the r-GO is in beneficial for energy attenuation, while the increasing conductivity would increase the energy conversion effectiveness of the composites. Therefore, the results shown in this work indicate the fundamental principles for achieving high-performance EMI shielding materials.

Experimental

Materials The graphite powder (flake graphite, grade 325) was purchased from Haida Corporation (Qingdao, China). The chemical reagents of $KMnO_4$ (Analysis), THF (Analysis), H_2O_2 (30 wt.%), hydrazine (80 wt.%), ammonia (25 wt.%), HNO_3 (65 wt.%), HCl (35 wt.%) and H_2SO_4 (96 wt.%) were obtained from the Beijing chemical factory without further purification. Deionized water was used in all the experiments. The commercially available graphite powders were first heated on 573 K for drying.

GNs The as-supplied graphite sample was processed by a combination of alcohol and oxidative acid treatments to form GNs.[29]

GO According to the modified Hummers' method,[35,57] GO is obtained by the harsh oxidation of the natural graphite powder.

r-GOs The r-GO powder was reduced from GO with hydrazine hydrate using the Wallace method and then freeze-dried.[36]

Composites In a typical experiment, the r-GOs (5, 10, 15 and 20 wt. %) and paraffin wax (95, 90, 85 and 80 wt. %) were added into the THF with vigorous stirring to evaporate the solution completely. A portion of the prepared mixture was pressed into toroidal shape (Φ_{out}: 7.03 mm; Φ_{in}: 3.00 mm). It should be noted that the test samples are adjusted with almost the same thickness ~2 mm. Similarly, the GN/paraffin wax composites with the same mass ratio were fabricated via the same process as described above.

Measurement XRD measurements were performed on an X´Pert PRO system (Cu-Kα). AFM images are obtained on a Veeco Dimension FastScan system. TEM images were got on a JEM-2100 TEM system, coupled with carbon- or holey carbon-coated copper grids. SSA curves were obtained on an ASAP 2020 surface area and porosity analyzer. Both the samples were degassed at 393 K for 4 h in a vacuum oven prior to the adsorption experiments. XPS spectrum was measured on a PHI Quantera system with a C60 ion gun. DC conductivity of the composites was measured on a Keithley 4200-SCS semiconductor characterization system. The relative permittivity was measured on an Anritsu 37269D vector network analyzer by the coaxial method. EMI SE of the composites was calculated by related scattering data.

Conclusions

In conclusion, r-GO composites exhibit higher dielectric properties and enhanced microwave attenuation performances than the GN composites. The thinner thickness, clustered defects and residual bonds enhance the polarization of the r-GO. Meanwhile, the increased polarization and scattering loss coupled with higher conductivity increase the dielectric loss and energy attenuation of the r-GO composites, which endows the r-GO composites with high dielectric loss and EMI shielding performance. The loss tangent values are significantly raised. EMI SE is ~3–10 times higher than that of GN composites with the same mass ratio. These results suggest that the r-GO composites are ideal candidates for applications in microwave attenuation. As the thinnest and most lightweight material around carbon family, the foreground of the r-GOs in military, industrial, office and home fields could be forecasted.

Acknowledgements

Thanks Dr. Zhuo Chen and Dr. Jia-song Zhang in Beijing Institute of Technology (BIT) for the DC conductivity test. Thanks Dr. Miao-miao Jin in BIT for the BET test. This work was supported by the National Science Foundation of P. R. China (Grant No. 51072024, 51372282 and 51132002).

Notes and references

[a] School of Material Science and Engineering, Beijing Institute of Technology, Beijing 100081, PR China

[b] School of Science, Minzu University of China, Beijing 100081, PR China

* Address correspondence to: E-mail: caomaosheng@bit.edu.cn; hbjin@bit.edu.cn; wzhwangmuc@163.com.
[1] These authors contributed equally to this work.

1 G. Z. Wang, Z. Gao, S. W. Tang, C. Q. Chen, F. F. Duan, S. C. Zhao, S. W. Lin, Y. H. Feng, L. Zhou and Y. Qin, *ACS Nano*, 2012, *6*, 11009.
2 W. L. Song, M. S. Cao, M. M. Lu, J. Liu, J. Yuan and L. Z. Fan, *J. Mater. Chem. C*, 2013, *1*, 1846.
3 B. Wen, M. S. Cao, Z. L. Hou, W. L. Song, L. Zhang, M. M. Lu, H. B. Jin, X. Y. Fang, W. Z. Wang and J. Yuan, *Carbon*, 2013, *65*, 124.
4 N. J. Tang, W. Zhong, C. T. Au, Y. Yang, M. G. Han, K. J. Lin and Y. W. Du, *J. Phys. Chem. C*, 2008, *112*, 19316.
5 M. S. Cao, W. L. Song, Z. L. Hou, B. Wen and J. Yuan, *Carbon*, 2010, *48*, 788.
6 Z. J. Wang, L. N. Wu, J. G. Zhou, W. Cai, B. Z. Shen and Z. H. Jiang, *J. Phys. Chem. C*, 2013, *117*, 5446.
7 Y. Z. Long, Z. J. Chen, X. T. Zhang, J. Zhang and Z. F. Liu, *Appl. Phys. Lett.*, 2013, *85*, 1796.
8 Y. P. Duan, S. H. Liu, G. Q. Wang, H. T. Guan and B. Wen, *J. Appl. Polym. Sci.*, 2006, *102*, 1839.
9 Y. P. Duan, Y. Yang, M. He, S. H. Liu, X. D. Cui and H. F. Chen, *Journal of Physics D: Applied*, 2008, *41*, 125403.
10 C. N. R. Rao, A. K. Sood, K. S. Subrahmanyam and A. Govindaraj, *Angew. Chem. Int. Ed.*, 2009, *48*, 7752.
11 A. H. Castro-Neto, F. Guinea, N. M. R. Peres, K. S. Novoselov and A. K. Geim, *Rev. Mod. Phys.*, 2009, *81*, 109.
12 D. R. Dreyer, S. Park, C. W. Bielawski and R. S. Ruoff, *Chem. Soc. Rev.*, 2010, *39*, 228.
13 S. Stankovich, D. A. Dikin, G. H. B. Dommett, K. M. Kohlhaas, E. J. Zimney, E. A.Stach, R. D. Piner, S. T. Nguyen and R. S. Ruoff, *Nature*, 2006, *442*, 282.
14 L. Z. Fan, J. L. Liu, R. Ud-Din, X. Q. Yan and X. H. Qu, *Carbon*, 2012, *50*, 3724.
15 Y. Z. Long, M. Yu, B. Sun, C. Z. Gu and Z. Y. Fan, *Chem. Soc. Rev.*, 2012, *41*, 4560.
16 Y. Huang, J. J. Liang and Y. S. Chen, *Small*, 2012, *8*, 1805.
17 F. Y. Su, C. H. You, Y. B. He, W. Lv, W. Cui, F. M. Jin, B. H. Li, Q. H. Yang and F. Y. Kang, *J. Mater. Chem.*, 2010, *20*, 9644.
18 S. T. Lu, Y. W. Cheng, X. H. Wu and J. Liu, *Nano Lett.*, 2013, *13*, 2485.
19 X. H. Rui, J. X. Zhu, D. Sim, C. Xu, Y. Zeng, H. H. Hng, T. M. Lim and Q. Y. Yan, *Nanoscale*, 2011, *3*, 4752.
20 J. Zhu, D. N. Lei, G. H. Zhang, Q. H. Li, B. G. Lu and T. H. Wang, *Nanoscale*, 2013, *5*, 5499.
21 N. Li, G. M. Zhou, R. P. Fang, F. Li and H. M. Cheng, *Nanoscale*, 2013, *5*, 7780.
22 D. Z. Chen, H. Y. Quan, J. F. Liang and L. Guo, *Nanoscale*, 2013, *5*, 9684.
23 X. Y. Yan, X. L. Tong, Y. F. Zhang, X. D. Han, Y. Y. Wang, G. Q. Jin, Y. Qin and X. Y. Guo, *Chem. Commun.*, 2012, *48*, 1892.
24 S. D. Yang, C. M. Shen, Y. Y. Liang, H. Tong, W. He, X. Z. Shi, X. G. Shen and H. J. Gao, *Nanoscale*, 2011, *3*, 3277.
25 F. He, N. Niu, F. Y. Qu, S. Q. Wei, Y. J. Chen, S. L. Gai, P. Gao, Y. Wang and P. Yang, *Nanoscale*, 2013, *5*, 8507.
26 Q. Feng, Q. Q. Cao, M. Li, F. C. Liu, N. J. Tang and Y. W. Du, *Appl. Phys. Lett.*, 2013, *102*, 013111.
27 R. Liu, X. W. Fu, J. Meng, Y. Q. Bie, D. P. Yu and Z. M. Liao, *Nanoscale*, 2013, *5*, 5294.
28 L. L. Tian, P. Anilkumar, L. Cao, C. Y. Kong, M. J. Meziani, H. J. Qian, L. M. Veca, T. J. Thorne, K. N. Tackett, T. Edwards and Y. P. Sun, *ACS Nano*, 2011, *5*, 3052.
29 L. M. Veca, M. J. Meziani, W. Wang, X. Wang, F. S. Lu, P. Y. Zhang, Y. Lin, R. Fee, J. W. Connell and Y. P. Sun, *Adv. Mater.*, 2009, *21*, 2088.
30 J. J. Liang, Y. Wang, Y. Huang, Y. F. Ma, Z. F. Liu, J. M. Cai, C. D. Zhang, H. J. Gao and Y. S. Chen, *Carbon*, 2009, *47*, 922.
31 X. Bai, Y. H. Zhai and Y. Zhang, *J. Phys. Chem. C*, 2011, *115*, 11673.
32 K. Singh, A. Ohlan, V. H. Pham, R. Balasubramaniyan, S. Varshney, J. Jang, S. H. Hur, W. M. Choi, M. Kumar, S. K. Dhawan, B. S. Kong and J. S. Chung, *Nanoscale*, 2013, *5*, 2411.
33 P. Saini, M. Arora, G. Gupta, B. K. Gupta, V. N. Singh and V. Choudhary, *Nanoscale*, 2013, *5*, 4330.
34 B. Wen, M. S. Cao, M. M. Lu, W. Q. Cao, H. L. Shi, J. Liu, X. X. Wang, H. B. Jin, X. Y. Fang, W. Z. Wang and J. Yuan, *Adv. Mater.*, *2014*, DOI: ADMA201400108.
35 W. S. Hummers and R. E. Offeman, *J. Am. Chem. Soc.*, 1958, *80*, 1339.
36 W. Gao, L. B. Alemany, L. J. Ci and P. M. Ajayan, *Nat. Chem.*, 2009, *1*, 403.
37 G. X. Wang, J. Yang, J. S. Park, X. L. Gou, B. Wang, H. Liu and J. Yao, *J. Phys. Chem. C*, 2008, *112*, 8192.
38 H. L. Shi, G. L. Zhang, B. Zou, M. T. Luo and W. Z. Wang, *Microsc. Res. Tech.*, 2013, *76*, 641.
39 P. C. P. Watts, W. K. Hsu, A. Barnes and B. Chambers, *Adv. Mater.*, 2003, *15*, 600.
30 T. Y. Kim, H. W. Lee, J. E. Kim and K. S. Suh, *ACS Nano*, 2010, *4*, 1612.
41 C. Gomez-Navarro, R. T. Weitz, A. M. Bittner, M. Scolari, A. Mews, M. Burghard and K. Kern, *Nano Lett.*, 2007, *7*, 3499.
42 A. B. Kaiser and V. Skakalova, *Chem. Soc. Rev.*, 2011, *40*, 3786.
43 H. B. Zhang, Q. Yan, W. G. Zheng, Z. X. He and Z. Z. Yu, *ACS Appl. Mater. Interfaces.*, 2011, *3*, 918.
44 D. D. L. Chung, *Carbon*, 2001, *39*, 279.
45 M. S. Cao, J. Yang, W. L. Song, D. Q. Zhang, B. Wen, H. B. Jin, Z. L. Hou and J. Yuan, *ACS Appl. Mater. Interfaces.*, 2012, *4*, 6949.
46 N. J. Tang, Y. Yang, K. J. Lin, W. Zhong, C. T. Au and Y. W. Du, *J. Phys. Chem. C*, 2008, *112*, 10061.
47 W. L. Song, M. S. Cao, M. M. J. Lu, Yang, H. F. Ju1, Z. L. Hou, J. Liu, J. Yuan and L. Z. Fan, *Nanotechnology*, 2013, *24*, 115708.
48 V. K. Singh, A. Shukla, M. K. Patra, L. Saini, R. K. Jani, S. R. Vadera and N. Kumar, *Carbon*, 2012, *50*, 2202.
49 H. L. Xu, H. Bi and R. B. Yang, *J. Appl. Phys.*, 2012, *111*, 07A522.
50 Y. Huang, N. Li, Y. F. Ma, F. Du, F. F. Li, X. B. He, X. Lin, H. J. Gao and Y. S. Chen, *Carbon*, 2007, *45*, 1614.
51 J. C. Wang, C. S. Xiang, Q. Liu, Y. B. Pan and J. K. Guo, *Adv. Funct. Mater.*, 2008, *18*, 2995.
52 N. Li, Y. Huang, F. Du, X. B. He, X. Lin, H. J. Gao, Y. F. Ma, F. F. Li, Y. S. Chen and P. C. Eklund, *Nano Lett.*, 2006, *6*, 1141.
53 H. M. Kim, K. Kim, C. Y. Lee, J. Joo, S. J. Cho, H. S. Yoon, D. A. Pejaković, J. W. Yoo and A. J. Epstein, *Appl. Phys. Lett.*, 2004, *84*, 589.
54 B. W. Li, Y. Shen, Z. X. Yue and C. W. Nan, *Appl. Phys. Lett.*, 2006, *89*, 132504.
55 H. L. Yu, T. S. Wang, B. Wen, M. M. Lu, Z. Xu, C. L. Zhu, Y. J. Chen, X. Y. Xue, C. W. Sun and M. S. Cao, *J. Mater. Chem.*, 2012, *22*, 21679.
56 E. Vazquez and M. Prato, *ACS Nano*, 2009, *3*, 3819.
57 L. J. Cote, F. Kim and J. X. Huang, *J. Am. Chem. Soc.*, 2009, *131*, 1043.